The Spatial and Temporal Structure of ENSO Nonlinearity

ADAM HUGH MONAHAN

School of Earth and Ocean Sciences, University of Victoria, Victoria, British Columbia, and Canadian Institute for Advanced Research, Earth Systems Evolution Program, Toronto, Ontario, Canada

AIGUO DAI

National Center for Atmospheric Research, Boulder, Colorado*

(Manuscript received 21 October 2003, in final form 9 February 2004)

ABSTRACT

The spatial structure of asymmetries in sea surface temperature (SST) and surface air temperature (SAT) between average El Niño and La Niña events is considered. It is demonstrated that in historical SST and SAT reconstructions, the anomaly spatial pattern that changes sign between El Niño and La Niña events (the ''linear'' signal) strongly resembles that of principal component analysis (PCA) mode 1, while that which does not change sign (the ''nonlinear'' signal) resembles the pattern of PCA mode 2. The linear and nonlinear patterns also strongly resemble the standard deviation and skewness fields, respectively. Furthermore, temporal subsampling of long (130 yr) SST reconstructions suggests that the magnitude of the nonlinear signal and its similarity to PCA mode 2 are functions of the strength of ENSO, as measured by the standard deviation of the PCA mode-1 time series. Finally, it is found that of several coupled general circulation models (GCMs) considered, the spatial and temporal structure of the El Niño–La Niña asymmetry is captured only by the GFDL R30 model, despite large biases in its covariance structure.

1. Introduction

El Niño–Southern Oscillation (ENSO) is the dominant mode of climate variability on interannual timescales, with effects that extend from the tropical Pacific to the entire globe (Philander 1990). While not perfectly periodic, ENSO variability is sufficiently regular to suggest that the underlying dynamics are characterized by a relatively small number of degrees of freedom, perhaps subject to fluctuating atmospheric forcing. In particular, Penland and Sardeshmukh (1995) found empirically that increasing beyond 15 the number of sea surface temperature (SST) principal components retained in their linear inverse forecast model did not improve the model's forecast skill, suggesting that ENSO may be characterized by a relatively low-dimensional attractor that can be embedded in this 15-dimensional Cartesian space. The characterization of this presumed ENSO attractor is important both for guiding the theoretical understanding of ENSO and for assessing the ability of coupled general circulation models (GCMs) to represent this phenomenon.

While considerable progress in understanding the dynamics of ENSO has been made with linearized models of the tropical Pacific (e.g., Penland and Sardeshmukh 1995; Kleeman and Moore 1997; Thompson and Battisti 2000), the distribution of SSTs is manifestly non-Gaussian. In particular, the Niño-3 index is positively skewed, so that strong El Niño events are associated with larger SST anomalies than strong La Niña events (Hannachi et al. 2003; An and Jin 2004), although the statistical significance of this skewness has been questioned (Ewald et al. 2004); the tropical Pacific SST field displays significant skewness (Burgers and Stephenson 1999); and the composite SST anomaly patterns for El Niño and La Niña are not mirror images (Hoerling et al. 1997; Rodgers et al. 2004). Furthermore, Monahan (2001) demonstrated that the leading two principal component analysis (PCA) time series of tropical Pacific SST for the period 1950–98 are not statistically independent, despite being linearly uncorrelated by construction. This nonlinear coupling of the PCA modes manifests itself in the difference in spatial structure between El Niño and La Niña composite maps: the pattern that changes sign between El Niño and La Niña, characteristic of the linear component of the dynamics, is essentially identical to the spatial structure of PCA mode

* The National Center for Atmospheric Research is sponsored by the National Science Foundation.

Corresponding author address: Dr. Adam Monahan, School of Earth and Ocean Sciences, University of Victoria, P.O. Box 3055, STN CSC, Victoria, BC V8W 3P6, Canada.
E-mail: monahana@uvic.ca

1, while the pattern that does not change sign, reflecting nonlinearities in the dynamics, is essentially identical to PCA mode 2.

The tropical Pacific is a tremendously important component of the climate system, but has been poorly observed. Consequently, long-term gridded SST datasets can only be obtained as historical reconstructions in which statistical algorithms are used to interpolate between sparsely sampled observations. The present study extends Monahan (2001), considering El Niño–La Niña asymmetry in several different historical SST and surface air temperature (SAT) reconstructions. In an earlier analysis of historical SST reconstructions, Hurrell and Trenberth (1999) demonstrated significant differences between the first- and second-order statistics of these datasets, as well as differences in large-scale trends. Similarities and differences in nonlinear structure, which are the focus of the present study, were not considered by Hurrell and Trenberth (1999).

Finally, the accurate simulation of ENSO by coupled GCMs is an important measure of their ability to represent the earth's climate system. Intercomparison studies have investigated the ability of different GCMs to simulate the mean and variance of the tropical Pacific system (Latif et al. 2001; AchutaRao and Sperber 2002; Davey et al. 2002), as well as their ability to simulate the skewness of the Niño-3 index (Burgers and Stephenson 1999; Hannachi et al. 2003; Rodgers et al. 2004). This study will consider the extent to which four state-of-the-art coupled GCMs can simulate the spatial structure of ENSO nonlinearity, as characterized in Monahan (2001).

The datasets considered in this study are described in section 2. The analysis of historical SST and SAT reconstructions is detailed in section 3, and that of the coupled GCMs is detailed in section 4. A discussion of the results is presented in section 5, and a summary and conclusions are given in section 6.

2. Data

This study focuses on the tropical Pacific, defined as 20°N–20°S, 125°E–65°W. Five monthly average SST reconstructions are considered: the United Kingdom Met Office (UKMO) Hadley Centre Sea Ice and SST dataset (HadISST; Rayner et al. 2003); the Lamont-Doherty Earth Observatory reconstruction by Kaplan et al. [1998; data available from the National Oceanic and Atmospheric Administration–Cooperative Institute for Research in Environmental Sciences (NOAA–CIRES) Climate Diagnostics Center online at http://www.cdc.noaa.gov/] and the National Climatic Data Center (NCDC) Extended Reconstruction SST versions 1 (ERSST.v1; Smith and Reynolds 2003) and 2 (ERSST.v2; Smith and Reynolds 2004; data available online at http://www1.ncdc.noaa.gov/pub/data/ersst) and Optimum Interpolation (OI) SST datasets [Smith et al. (1996); data available online from the NCAR Data Support Section (DSS) at http://dss.ucar.ed/datasets/ds277.0/data/recon/]. Also, two monthly averaged SAT reconstructions are considered from the reanalysis projects of the National Centers for Environmental Prediction–National Center for Atmospheric Research (NCEP–NCAR; Kalnay et al. 1996; data available online at http://www.cdc.noaa.gov/) and the European Centre for Medium-Range Weather Forecasts (ECMWF) Re-Analysis (ERA-40; Simmons and Gibson 2000; data available online at http://data.ecmwf.int/data/d/era40/).

These historical reconstructions differ considerably in the periods covered and in the algorithms used to produce gridded estimates of sparsely sampled fields. The SST reconstructions use multivariate statistical schemes to objectively interpolate observed SSTs onto regular latitude–longitude grids; no explicit dynamical information is used in these reconstructions. Conversely, the reanalysis SAT fields are produced using dynamical–statistical models so as to be optimally consistent with both observations and atmospheric dynamics, as represented by the atmospheric GCMs used in the reanalyses. These GCMs are themselves driven by reconstructed SST fields: a combination of the NCDC OI SST reconstruction and UKMO Global Sea Ice and SST dataset (GISST; an earlier version of HadISST) for the NCEP–NCAR reanalysis, and a combination of HadISST and Reynolds OI SST for the ERA-40 reanalysis. While the raw observations entering these reconstructions are similar, there are significant differences among the reconstruction algorithms (e.g., Hurrell and Trenberth 1999; Smith and Reynolds 2004).

Sea surface temperature datasets from four coupled GCM control simulations are considered. These models are the Geophysical Fluid Dynamics Laboratory (GFDL) R30 coupled climate model (Delworth et al. 2002; data available online at http://nomads.gfdl.noaa.gov/), the Hadley Centre HadCM3 model (Collins et al. 2001), the Department of Energy (DOE) Parallel Climate Model (PCM; Washington et al. 2000; Dai et al. 2001), and the NCAR Community Climate System Model (CCSM; Blackmon et al. 2001).

For each dataset, anomaly fields were produced by subtracting the long-term average seasonal cycle at each grid point. No other preprocessing of the data was carried out prior to the statistical analyses described in the subsequent sections. Table 1 summarizes the resolutions and durations of the reconstructed and simulated datasets considered in this study.

3. El Niño–La Niña asymmetry in historical reconstructions

We will first focus on the El Niño–La Niña asymmetry in the HadISST SST reconstruction. The leading two PCA spatial patterns (EOF_1 and EOF_2, respectively) of the HadISST SST are displayed in Fig. 1; a scatterplot of the corresponding time series (PC_1 and PC_2, respectively) is displayed in Fig. 2. As discussed in Monahan

TABLE 1. Details of the datasets considered in this study.

	Field	Resolution	Record length
HadISST	SST	2° × 2°	1871–2000
Kaplan	SST	5° × 5°	1871–2000
ERSST.vl	SST	2° × 2°	1871–2000
ERSST.v2	SST	2° × 2°	1871–2000
OI	SST	2° × 2°	1950–2000
NCEP–NCAR	SAT	1.875° × 1.9°	1948–2002
ERA-40	SAT	2.5° × 2.5°	1957–2002
GFDL	SST	1.875° × 2.24°	400 yr
HadCM3	SST	2.5° × 2.5°	1041 yr
DOE PCM	SST	2.8° × 2.8°	1000 yr
NCAR CCSM	SST	2.8° × 2.8°	999 yr

(2001), it is evident from Fig. 2 that the two PC time series are not independent, despite being linearly uncorrelated by construction. In particular, PC_2 tends to take positive values for large positive and negative excursions of PC_1, reflecting the fact that, on average, the amplitudes of warm anomalies along the equator east of 150°W during El Niño events are greater than those of the cold anomalies during La Niña events. This asymmetry can be quantified by defining as an ENSO index the PC_1 time series, normalized by its standard deviation; this ENSO index is highly correlated ($r = 0.96$) with the standard Niño-3.4 index. An El Niño composite map is calculated by averaging the SST anomaly over all months for which the ENSO index exceeds 1; similarly, a La Niña composite map is obtained by averaging over all months for which the ENSO index is <-1. The asymmetry between these composites can be characterized by defining the antisymmetric and symmetric components as in Monahan (2001): assuming that

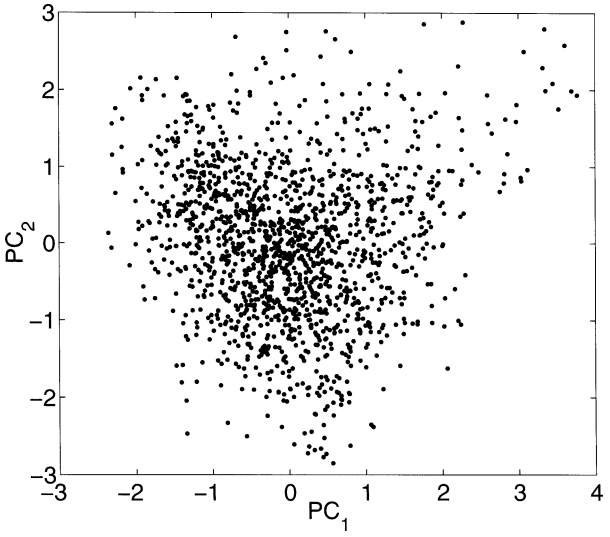

FIG. 2. Scatterplot of HadISST SST PC_1 with PC_2. For consistency with Fig. 1, both time series have been normalized to unit std dev.

the field $\mathbf{X}(t)$ (in this case, the SST) has a quadratic dependence on the index $\lambda(t)$ (in this case, the ENSO index), so that

$$\mathbf{X}(t) = \mathbf{a}^{(0)} + \mathbf{a}^{(1)}\lambda(t) + \mathbf{a}^{(2)}\lambda^{(2)}(t) + \boldsymbol{\epsilon}(t), \qquad (1)$$

where $\boldsymbol{\epsilon}$ is a residual, the maps $\mathbf{a}^{(1)}$ and $\mathbf{a}^{(2)}$ represent, respectively, the spatial patterns in $\mathbf{X}$ that reverse sign and retain the same sign under a change in sign of λ. Without any loss of generality, we will assume that the time averages of $\mathbf{X}$ and λ both vanish. Denoting time averaging by angle brackets $\langle \cdot \rangle$, and averaging over excursions of λ beyond positive and negative thresholds

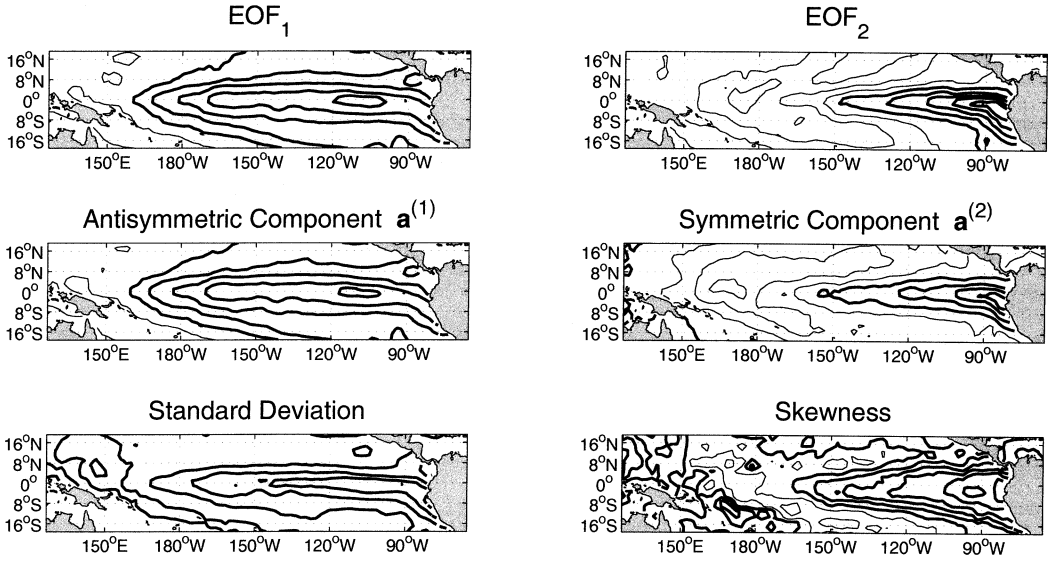

FIG. 1. Maps of HadISST SST EOF_1 (contours . . . −0.1°, 0.1°, 0.3°C, . . .), SST EOF_2 (contours . . . −0.05°, 0.05°, 0.15°C, . . .), the antisymmetric component of the ENSO composite $\mathbf{a}^{(1)}$ (contours . . . −0.1°, 0.1°, 0.3°C, . . .), the symmetric component of the ENSO composite $\mathbf{a}^{(2)}$ (contours −0.02°, 0.02°, 0.06°C, . . .), the SST std dev (contours 0.1°, 0.3°C, . . .), and the SST skewness (contours . . . −0.1, 0.1, 0.3, . . .).

of +1 and −1 (by which the composites are defined) by the operators $\langle \cdot \rangle_+$ and $\langle \cdot \rangle_-$, respectively, then the maps $\mathbf{a}^{(1)}$ and $\mathbf{a}^{(2)}$ (denoted the antisymmetric or linear, and symmetric or nonlinear components of the composite, respectively) are given by

$$\mathbf{a}^{(1)} = \frac{1}{\Delta}[(\langle\lambda^2\rangle_- - \langle\lambda^2\rangle)\langle\mathbf{X}\rangle_+ - (\langle\lambda^2\rangle_+ - \langle\lambda^2\rangle)\langle\mathbf{X}\rangle_-] \quad (2)$$

$$\mathbf{a}^{(2)} = \frac{1}{\Delta}[-\langle\lambda\rangle_-\langle\mathbf{X}\rangle_+ + \langle\lambda\rangle_+\langle\mathbf{X}\rangle_-], \quad (3)$$

where

$$\Delta = \langle\lambda\rangle_+(\langle\lambda^2\rangle_- - \langle\lambda^2\rangle) - \langle\lambda\rangle_-(\langle\lambda^2\rangle_+ - \langle\lambda^2\rangle). \quad (4)$$

Note that in principle $\mathbf{a}^{(1)}$ and $\mathbf{a}^{(2)}$ can be estimated directly from (1) by minimizing $\langle\boldsymbol{\epsilon}^2\rangle$; however, because this model was introduced as a means of interpreting the El Niño and La Niña composites, the estimators (2) and (3) will be used in the present analysis.

The statistical model (1) was designed to be a minimal nonlinear model of the dependence of the field $\mathbf{X}$ on the index λ; it is not physically motivated, but rather corresponds to the two leading terms of a Taylor series expansion. In the absence of any a priori assumptions about the distributions of $\mathbf{X}$ and λ, nothing can be said about the distribution of the residuals $\boldsymbol{\epsilon}$ except that, by construction of the estimators (2) and (3), $\langle\boldsymbol{\epsilon}\rangle_- = \langle\boldsymbol{\epsilon}\rangle_+ = \mathbf{0}$. Because this study is an exploratory analysis of non-Gaussian structure in $\mathbf{X}$ and λ, it is not appropriate to make any a priori assumptions about their distributions. It is worth noting that the estimators (2) and (3) behave reasonably in simple limiting cases: in particular, if $\mathbf{a}^{(2)} = \mathbf{0}$, then by (1), $\langle\mathbf{X}\rangle_-$ and $\langle\mathbf{X}\rangle_+$ are proportional to $\langle\lambda\rangle_-$ and $\langle\lambda\rangle_+$, respectively, and the right-hand side of (3) is identically zero, regardless of the distribution of λ. Furthermore, if the distribution of λ is symmetric about its mean, then $\langle\lambda\rangle_- = \langle\lambda\rangle_+$ and $\langle\lambda^2\rangle_- = \langle\lambda^2\rangle_+$, so $\mathbf{a}^{(1)}$ and $\mathbf{a}^{(2)}$ reduce to the difference and sum maps defined in Hoerling et al. (1997) (up to constant scaling factors).

Clearly, $\mathbf{a}^{(1)}$ and $\mathbf{a}^{(2)}$ bear striking resemblances to EOF_1 and EOF_2 (Fig. 1); the respective pattern correlations are 0.99 and 0.88. Furthermore, the standard deviation and skewness fields of SST (Fig. 1) resemble EOF_1 and EOF_2, respectively (the pattern correlations are 0.91 and 0.81). The skewness

$$s = \frac{\langle(y - \langle y\rangle)^3\rangle}{[\langle(y - \langle y\rangle)^2\rangle]^{3/2}}, \quad (5)$$

or normalized third moment, of a variable y is a measure of the asymmetry of its probability distribution. The structure of both $\mathbf{a}^{(2)}$ and the SST skewness field reflect the propensity for PC_2 to take positive values when PC_1 is strongly positive or negative; that is, they both reflect the nonlinear coupling between EOF modes 1 and 2 evident in Fig. 2. The fact that the skewness field is not identical to EOF_2 is a consequence of the fact that PC_1, like the Niño-3 and Niño-3.4 indices, is itself somewhat positively skewed.

TABLE 2. Pattern correlation between EOF_2 and $\mathbf{a}^{(2)}$ (the symmetric component of the ENSO composite), and the relative magnitude of the symmetric and antisymmetric components of the composite, for the SST and SAT reconstructions and simulations considered in this study. Values in parentheses correspond to estimates of these quantities over the period from 1950 to 2000.

Dataset	Pattern correlation	$\|\mathbf{a}^{(2)}\|/\|\mathbf{a}^{(1)}\|$
HadISST	0.88 (0.93)	0.12 (0.20)
Kaplan	0.75 (0.84)	0.25 (0.19)
ERSST.v1	0.13 (0.65)	0.05 (0.08)
ERSST.v2	0.64 (0.79)	0.11 (0.16)
OI	0.84	0.16
NCEP–NCAR	0.79	0.17
ERA-40	0.91	0.21
GFDL	0.75	0.13
HadCM3	0.28	0.08
DOE PCM	0.40	0.04
NCAR CCSM	0.17	0.07

At this point it is useful to contrast the nonlinear statistical model (1) with the linear two-PCA model:

$$\mathbf{X}(t) = (\mathrm{EOF}_1)\mathrm{PC}_1(t) + (\mathrm{EOF}_1)\mathrm{PC}_2(t) + \boldsymbol{\epsilon}_{\mathrm{PCA}}(t). \quad (6)$$

This linear model will explain a higher proportion of variance than the nonlinear model, as it involves two expansion time series rather than one, but it does not take advantage of the dependence between PC_1 and PC_2 evident in Fig. 2. Having defined λ as PC_1, it is not surprising that $\mathbf{a}^{(1)}$ should be identical to EOF_1. The strong similarity of $\mathbf{a}^{(2)}$ and EOF_2, on the other hand, is a nontrivial result of two factors: 1) the positive skewness of λ is weak enough that λ and λ^2 are only weakly correlated, and 2) the asymmetries in SST and SAT between positive and negative excursions of λ are strong. If either of these two conditions did not hold, $\mathbf{a}^{(2)}$ could in principle project strongly on to EOF_1 or on to PCA modes 3 or higher.

Identical analyses to those performed on the HadISST SST reconstruction were carried out on the ERSST.v1, ERSST.v2, Kaplan, and OI SST reconstructions, and on the NCEP–NCAR and ERA-40 SAT reanalyses; the results are presented in Table 2. The spatial structures of the leading two PCA modes for each of these historical reconstructions were in good agreement with those shown in Fig. 1. Because the anomaly pattern of a PCA mode is only determined up to a sign, in these and all subsequent PC analyses this ambiguity was eliminated by ensuring that the anomaly patterns of the leading two PCA modes agree in sign with those displayed in Fig. 1. The strong spatial correlation between the symmetric component of the composite and EOF_2 is evident in all reconstructions except ERSST.v1. Furthermore, the ratio of the root-mean-squared amplitudes of $\mathbf{a}^{(1)}$ and $\mathbf{a}^{(2)}$, which measures the amplitude of the ENSO asymmetry rather than its pattern, is also indicated in Table 2. The

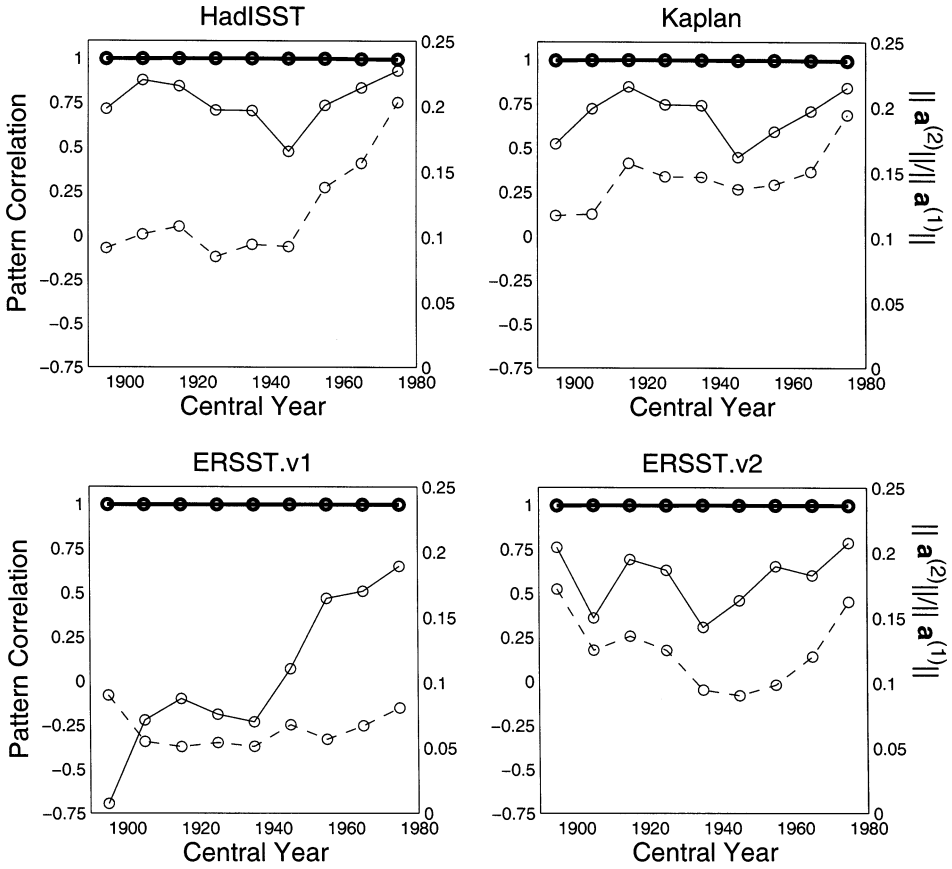

FIG. 3. Plots of the pattern correlation of EOF_1 with $\mathbf{a}^{(1)}$, the antisymmetric component of the ENSO composite (thick line); of the pattern correlation of EOF_2 with $\mathbf{a}^{(2)}$, the symmetric component of the ENSO composite (thin line); and of the ratio of the amplitude of $\mathbf{a}^{(2)}$ to that of $\mathbf{a}^{(1)}$ (dashed line), for each of the 50-yr subintervals. The circles correspond to the center of each subinterval.

amplitude of the symmetric component of the composite relative to the antisymmetric component for the ERSST.v1 is considerably less than that of all other reconstructions. The relatively high value of the ratio $\|\mathbf{a}^{(2)}\|/\|\mathbf{a}^{(1)}\|$ for the Kaplan SST reconstruction arises because a long-term trend in this dataset projects strongly onto EOF_2.

Results of an analysis of the HadISST, Kaplan, ERSST.v1, and ERSST.v2 SST reconstructions for the 1950–2000 period, corresponding roughly to the period covered by the OI reconstruction and the NCEP–NCAR and ERA-40 reanalyses, are presented in parentheses in Table 2. For each of these three reconstructions, the connection between $\mathbf{a}^{(2)}$ and EOF_2 is stronger in this last 50-yr period than it is over the complete 130-yr record; the increase in pattern correlation is marginal for the HadISST, ERSST.v2, and Kaplan reconstructions, but considerable for the ERSST.v1 reconstruction. The magnitude of $\mathbf{a}^{(2)}$ relative to $\mathbf{a}^{(1)}$ over this period is somewhat smaller for the Kaplan reconstruction, because the trend in PC_2 is weaker in the last 50 yr than it is over the entire record, and the ratio is considerably stronger for the HadISST and ERSST.v2 reconstructions. A small increase in the ratio of magnitudes of the symmetric and antisymmetric components of the composite is evident for the ERSST.v1 reconstruction, but the ratio is still small relative to other reconstructions of this period.

To examine temporal variations in the strength of the El Niño–La Niña asymmetry and its projection on EOF_2, each of the HadISST, ERSST.v1, ERSST.v2, and Kaplan SST reconstructions were split into a series of nine overlapping 50-yr subsets, with the central year increasing in 10-yr increments. For each of these data subsets, the annual cycles, principal components, and ENSO composites were calculated independently. Figure 3 plots the subset pattern correlations between EOF_1 and $\mathbf{a}^{(1)}$ and between EOF_2 and $\mathbf{a}^{(2)}$, as well as the subset ratios of the magnitude of $\mathbf{a}^{(2)}$ to that of $\mathbf{a}^{(1)}$, for each of the SST reconstructions. Clearly, for each of the SST reconstructions, the relationship between EOF_1 and the antisymmetric component of the ENSO composite is robust to the subsampling of the dataset. The relationship between EOF_2 and the symmetric component of the composite is more variable. The Kaplan, HadISST, and ERSST.v2 reconstructions display consistently

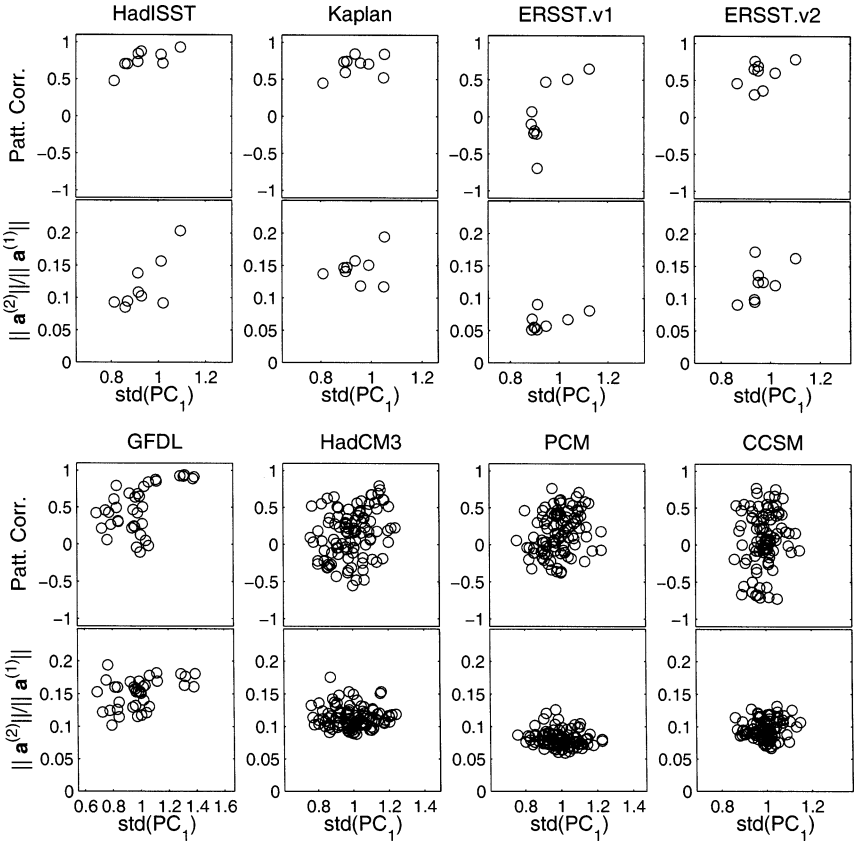

FIG. 4. Scatterplots of the std dev of SST PC_1 (normalized by the std dev of PC_1 for the entire record) vs (upper panels) the pattern correlation of SST EOF_2 with $\mathbf{a}^{(2)}$, the symmetric component of the ENSO composite, and vs (lower panels) the ratio of the magnitude of the symmetric component of the composite to the magnitude of the antisymmetric component of the composite, $\mathbf{a}^{(1)}$, for each of the 50-yr data subsets.

strong projections characterized by distinct interdecadal variability. However, the projection is only strongly positive for the ERSST.v1 reconstruction at the end of the record; for most of the period of the reconstruction, the projection is weak or, for the period 1871–1920, strongly negative. For the HadISST, ERSST.v2, and Kaplan reconstructions, the amplitude of the symmetric (i.e., nonlinear) component of the ENSO component relative to the antisymmetric (i.e., linear) component also displays interdecadal variability. This ratio is weak for the ERSST.v1, and displays considerably less interdecadal variability than the other reconstructions.

Interdecadal variations in the strength and structure of the El Niño–La Niña asymmetry in the HadISST, ERSST.v2, and Kaplan SST reconstructions appear to be connected to interdecadal variations in the strength of ENSO, as measured by the standard deviation of PC_1. This relationship is illustrated in Fig. 4. Note that in general both the strength of the asymmetry and the spatial correlation of $\mathbf{a}^{(2)}$ with EOF_2 increase with increases in std(PC_1). During periods in which ENSO variability is relatively weak (strong), the spatial structure of SST is relatively symmetric (asymmetric) between warm and cool events. Not surprisingly, such a clear relationship between the strength of ENSO and the character of its nonlinearity is absent in the ERSST.v1 SST reconstruction.

Thus, there is evidence in historical reconstructions of tropical Pacific SST and SAT for a coupling between PCA modes 1 and 2, such that the average ''linear'' component of ENSO variability is captured by EOF_1, while the average ''nonlinear'' component is strongly associated with EOF_2. This coupling of PCA modes is a nontrivial result, as they are by construction uncorrelated. In fact, this asymmetry between average El Niño and La Niña events is the most prominent feature of the description of the ENSO attractor beyond single indices such as Niño-3 or Niño-3.4. While there is considerable scatter in the El Niño–La Niña asymmetry between the different SST and SAT reconstructions, the qualitative similarities are strong, with the notable exception of the ERSST.v1 reconstruction; we will return to this point in section 5. Having diagnosed this relationship in historical datasets, we proceed to address the question of how will the El Niño–La Niña asymmetry is captured in coupled GCMs.

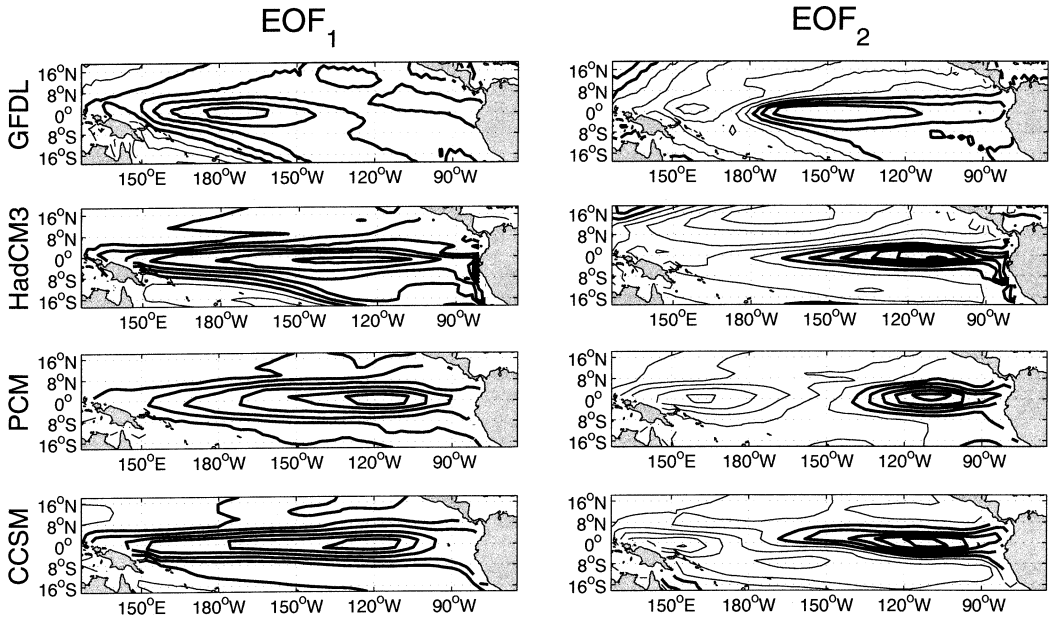

FIG. 5. Maps of EOF_1 (contours . . . −0.1°, 0.1°, 0.3°C, . . .) and EOF_2 (contours . . . −0.05°, 0.05°, 0.15°C, . . .) for modeled SST datasets. Thick (thin) lines denote positive (negative) contours.

4. Asymmetry in coupled GCMs

The analyses of the SST and SAT reconstructions described in the previous section were carried out on each of the GCM datasets described in section 2. Plots of SST EOF_1 and EOF_2 for each of the model datasets are given in Fig. 5, of the spatial structure of SST standard deviation and skewness are given in Fig. 6, and of the antisymmetric and symmetric components of the ENSO composites are given in Fig. 7. For each of the model datasets, the ENSO index was defined, as in section 3, as the leading principal component time series (normalized to unit variance), rather than as an ''area based'' index such as Niño-3.4. This is because the geographical distribution of SST variance in the model climates differs from that of observations; in particular, the GFDL SST variance maximum is located near the date line, far to the west of the observed maximum (Fig. 6). As the standard area-based indices are tuned to the observed variance distribution, by using an internally defined ENSO index, we are able to more directly study the asymmetries of the models' ENSO variabilities. It is clear from Figs. 5 and 7 that for each of the coupled GCMs, EOF_1 is essentially identical to the antisymmetric component of the ENSO composite; the pattern correlations were above 0.99 in all cases. On the other hand, the strong connection between EOF_2 and the symmetric component of the ENSO composite manifest in most of the historical reconstructions is captured only in the GFDL model although the maximum of the pattern is shifted to the central Pacific. From Fig. 7 and Table 2, it is clear that in the HadCM3, DOE PCM, and NCAR CCSM models, the symmetric components of the ENSO composites are weak and disorganized in comparison to those of the historical reconstructions and the GFDL simulation. Similarly, in each model there is a manifest similarity between SST EOF_1 and the SST standard deviation field (Fig. 6), but only the GFDL SST simulation is characterized by an organized skewness field that projects strongly onto EOF_2. For the other three models, the SST skewness fields are weak and spatially disorganized. It is worth noting that these results further reinforce the connection between the nonlinear coupling of EOF_1 and EOF_2, ENSO asymmetry, and SST skewness: only in the model with a strong asymmetry between average El Niño and La Niña SST patterns is the SST skewness strong and are the leading two EOF modes coupled. It should be noted that of the four coupled GCMs analyzed in this study, only the GFDL model uses surface flux adjustments to maintain a realistic climate. Interestingly, Rodgers et al. (2004) report an asymmetry between composite El Niño and La Niña fields in the flux-adjusted ECHO-G coupled GCM.

Figure 4 displays plots of the pattern correlation of EOF_2 with $\mathbf{a}^{(2)}$, and of the relative magnitude of the symmetric and antisymmetric components of the composite, for each 50-yr subset of the simulations. As was the case with the HadISST, ERSST.v2, and Kaplan historical SST reconstructions, the pattern correlation between EOF_2 and the antisymmetric component of the ENSO composite for the GFDL simulation is generally large and increases as the standard deviation of PC_1 increases. This behavior is not evident in the HadCM3, DOE PCM, or NCAR CCSM simulations. Furthermore, the increase in the magnitude of the nonlinear component of ENSO with the standard deviation of the ENSO

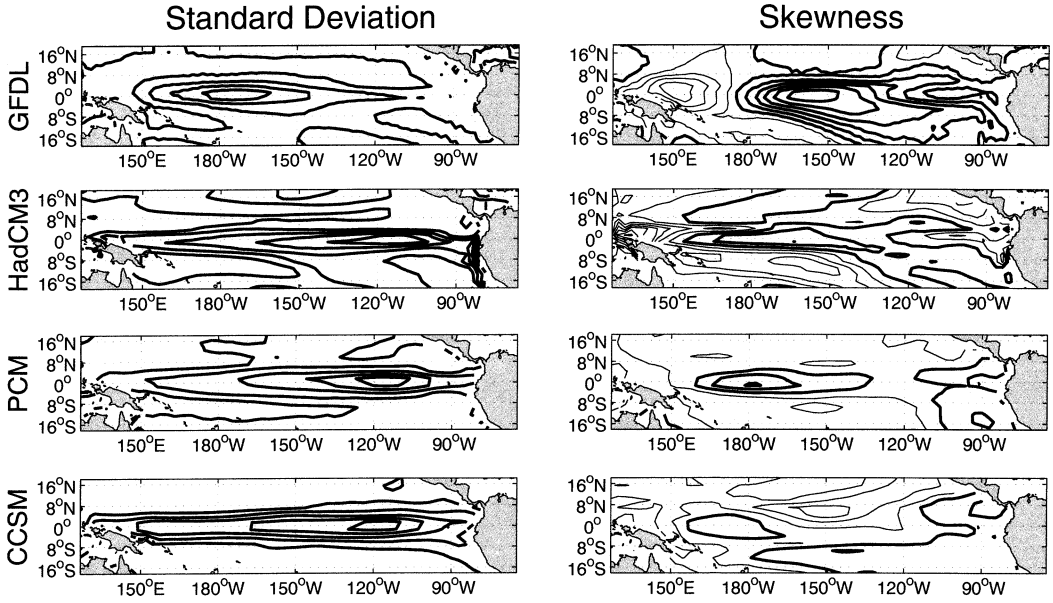

FIG. 6. Maps of std dev (contours 0.1°, 0.3°C, . . .) and skewness (contours . . .−0.1, 0.1, 0.3, . . .) for modeled SST datasets. Thick (thin) lines denote positive (negative) contours.

index observed in the HadISST, ERSST.v2, and Kaplan reconstructions is captured only in the GFDL simulation, and does not appear in the HadCM3, PCM, or CCSM models. Thus, of the four coupled GCM simulations considered, only that of the GFDL model reproduces the nonlinear coupling between EOF modes 1 and 2 evident in the historical SST and SAT reconstructions, despite its unrealistic covariance structure.

5. Discussion

The seven historical SST and SAT reconstructions considered in this study are in broad agreement that ENSO variability in the second half of the twentieth century was asymmetric between El Niño and La Niña events, with a linear structure of variability that projects strongly onto EOF_1 and a nonlinear structure that pro-

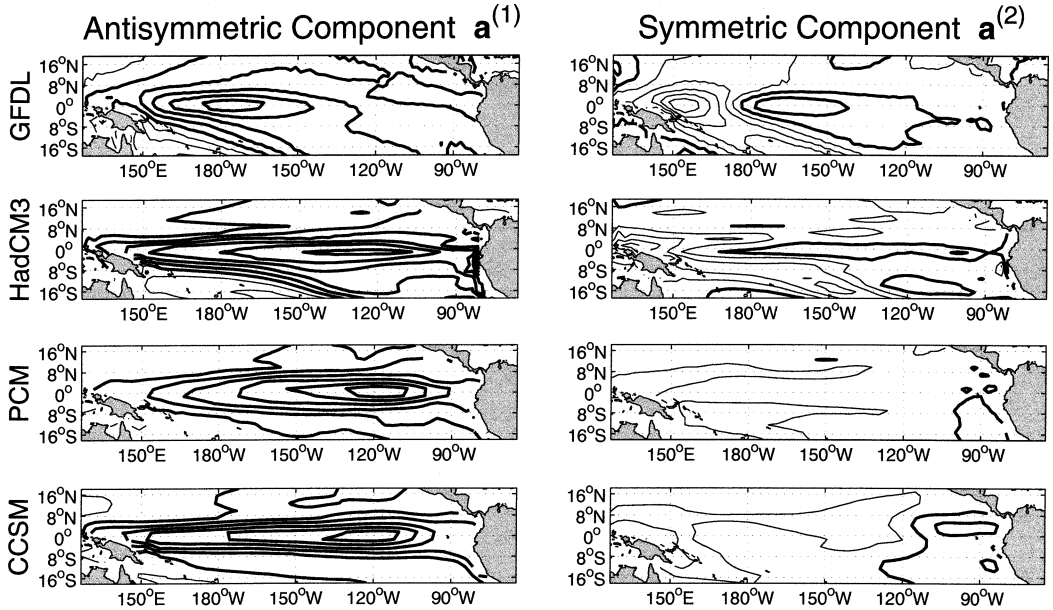

FIG. 7. Maps of the antisymmetric component of the ENSO composite [$\mathbf{a}^{(1)}$; contours . . .−0.1°, 0.1°, 0.3°C, . . .] and of the symmetric component [$\mathbf{a}^{(2)}$; contours . . .−0.02°, 0.02°, 0.06°C, . . .] for modeled SST datasets. Thick (thin) lines denote positive (negative) contours.

jects strongly onto EOF_2, consistent with the results of Monahan (2001). Furthermore, while the interdecadal variability of this nonlinear structure over the period 1871–2000 is broadly the same in the HadISST, Kaplan, and ERSST.v2 reconstructions, it is significantly different in the ERSST.v1 reconstruction, in which the magnitude of the symmetric component of the ENSO composite is too small and there is no clear relationship between $\mathbf{a}^{(2)}$ and EOF_2. In fact, the differences between ERSST.v1 and the other long-term SST reconstructions are not surprising given that ERSST.v1 has been shown to have a number of shortcomings, in particular in the tropical Pacific (Smith and Reynolds 2004). The ERSST.v2 reconstruction was developed to supersede ERSST.v1, and the present analysis demonstrates that the later reconstruction's characterisation of the nonlinear variability of the tropical Pacific SST is in good agreement with the HadISST and Kaplan reconstructions. The relatively small differences between the temporal and spatial structure of El Niño and La Niña as represented by the ERSST.v2, Kaplan, and HadISST reconstructions evident in Fig. 3 reflect differences in raw input data and reconstruction algorithms.

The possibility should be noted that the nonlinear structure in the HadISST, ERSST.v2, and Kaplan datasets is spurious, and is an artifact of the reconstruction algorithms. This is unlikely, because the algorithms used to reconstruct historical SST values over data-sparse regions assume stationarity of the covariance structure, but make no use of third- or higher-order moments. These algorithms would therefore be expected to bias the reconstructed data toward multivariate Gaussianity, and in fact for the Kaplan and HadISST reconstructions the magnitude of the symmetric composite is generally lower in the early part of the record than in the later. Therefore, it would not be expected that the robust connection between the spatial structure of the symmetric component of the ENSO composite and EOF_2 in the HadISST, ERSST.v2, and Kaplan reconstructions would arise as an artifact of the reconstruction algorithm.

Recent studies by Timmermann (2003) and Rodgers et al. (2004) have found evidence in long integrations of coupled GCMs (ECHAM4/OPYC3 and ECHO-G, respectively) that decadal modulations of the amplitude of ENSO are associated with decadal changes in the zonal tilt of the equatorial thermocline, such that large-amplitude ENSO events occur when the tilt is anomalously low. Furthermore, Rodgers et al. (2004) demonstrate that the El Niño and La Niña composites of the tropical Pacific SST and 20°C isotherm depth ($Z20$) fields from the flux-corrected ECHO-G GCM are characterized by asymmetries similar to those highlighted in the present study, and that the spatial patterns of these asymmetries strongly resemble those of the regression patterns of an index characterizing decadal variability in the equatorial thermocline tilt on SST and $Z20$. Rodgers et al. (2004) interpret these results as following from a hypothesized (but not explicitly demonstrated) proportionality of the magnitude of the ENSO asymmetry to the ENSO amplitude: during periods of large ENSO events, the asymmetry is presumed to be strong, so the asymmetry pattern should correlate well with an index of ENSO amplitude. The results of the present study provide evidence for this proposed proportionality, and for the suggestion that a portion of decadal variability in the tropical Pacific may result from nonlinear dynamics acting on ENSO time scales.

The historical SST and SAT reconstructions indicate that the dominant nonlinearity in ENSO variability can be associated with the nonlinear coupling of EOF modes 1 and 2, as manifest in the strong projection of the symmetric component of the ENSO composite onto EOF_2. The full spatial characterization of this nonlinearity therefore requires more than just a single index of ENSO variability, such as the Niño-3 or Niño-3.4 index (as in Hannachi et al. 2003). The importance of multiple indices for characterizing the ENSO attractor was stressed by Trenberth and Stepaniak (2001), who introduced the Trans-Niño Index (TNI) as a measure of the SST gradient between the eastern and the central Pacific. The correlation coefficient between the TNI and PC_2 for the HadISST SST reconstruction is 0.83; they describe similar variability. Trenberth and Stepaniak (2001) demonstrated the existence of significant lagged correlations between the Niño-3.4 and TNI indices (at least in the period before 1977). The present analysis demonstrates that the TNI is nonlinearly coupled to the Niño-3.4 index at zero month lag, and that the associated spatial pattern reflects the asymmetry in spatial structure of average El Niño and La Niña events. It should be emphasized here that this nonlinear coupling does not imply that the Niño-3.4 and TNI indices are redundant; the TNI time series contains information that is not present in the square of Niño-3.4. In particular, there are no strong lagged correlations between Niño-3.4 and its square. Nevertheless, EOF_2 (the TNI index, equivalently) is seen to play an important role in both the spatial and temporal structure of the ENSO attractor.

6. Summary and conclusions

The fact that tropical Pacific variability is not Gaussian, so that average El Niño and La Niña events are not mirror images, has been noted in several studies (Hoerling et al. 1997; Burgers and Stephenson 1999; Timmermann and Jin 2002; Hannachi et al. 2003; An and Jin 2004; Rodgers et al. 2004). It was suggested in Monahan (2001) that a basic feature of the ENSO attractor is that the asymmetry in SST anomaly spatial patterns between average El Niño and La Niña events is characterized by a nonlinear coupling of SST PCA modes 1 and 2, such that the ''nonlinear'' component of the anomaly patterns that does not change sign between warm and cold events projects strongly on the spatial pattern of PCA mode 2.

The present study has extended Monahan (2001) to

consider this asymmetry in seven different historical SST and SAT reconstructions, and in coupled GCM simulations. It was found that there is broad agreement among the historical reconstructions for this coupling of PCA modes in the 1950–2000 period. For three of the four SST reconstructions that extend back to 1871 (HadISST, Kaplan, and ERSST.v2), the connection between the nonlinear pattern and EOF_2 is apparent over the entire record. This connection is not evident in earlier parts of the ERSST.v1 reconstruction, but this reconstruction is known to be problematic in the tropical Pacific (Smith and Reynolds 2004); in fact, ERSST.v2 was developed as a replacement for ERSST.v1. Furthermore, subsampling the historical reconstructions into overlapping 50-yr intervals indicates in the HadISST, ERSST.v2, and Kaplan reconstructions that the strength of the nonlinearity and its identification with EOF_2 depend on the strength of ENSO. Finally, it is found that of four state-of-the-art coupled GCMs, only one (the GFDL R30 model) accurately simulates the nonlinear structure in ENSO, despite simulating the geographical distribution of variance relatively poorly. Simulated SSTs from HadCM3, CCSM, and PCM coupled models display skewness fields that are weak and disorganized compared to historical SST reconstructions and the GFDL simulations, and El Niño–La Niña composite patterns that are essentially mirror images. The divergence between the nonlinearity of ENSO as simulated in different coupled models is not surprising considering the continuing difficulties in representing the mean state and variance of the tropical Pacific (Latif et al. 2001; AchutaRao and Sperber 2002; Davey et al. 2002), and the fact that Burgers and Stephenson (1999) and Hannachi et al. (2003) found that most coupled GCMs do not accurately simulate the skewness of the Niño-3 index. It is worth noting that of the four coupled GCMs only the GFDL model uses surface flux adjustments to maintain a realistic climate. Recently, Rodgers et al. (2004) have reported an asymmetry in composite El Niño and La Niña SST patterns similar to that of the observations in the (flux adjusted) ECHO-G GCM. It would be interesting to see if this asymmetry is associated with a nonlinear coupling of PCA modes 1 and 2.

Historical SST reconstructions interpolate sparsely sampled observations using algorithms that make a number of highly questionable assumptions, such as stationarity of the covariance structure over the reconstruction period. Consequently, they are not ideally suited for analyses of climate variability, as Rayner et al. (2003) caution. Nevertheless, these are the only datasets presently available for the analysis of basin-scale variability in the tropical Pacific on multidecadal time scales. The possibility that the results of this analysis are to some extent spurious artifacts of the reconstruction algorithms must be admitted. However, given the agreement between all datasets for the 1950–2000 period; between the Kaplan, HadISST, and ERSST.v2 reconstructions for the 1871–2000 period; and the fact that all of the HadISST, Kaplan, and ERSST.v2 reconstructions make no use of statistical moments above the second and should therefore bias SST reconstructions toward Gaussianity, we believe it is unlikely that the results presented in section 3 are merely artifacts of the reconstruction.

The physical mechanisms responsible for the asymmetry between El Niño and La Niña are still unclear. Suggested mechanisms include nonlinearities in oceanic vertical temperature advection in the cold tongue region (Hannachi et al. 2003; An and Jin 2004), nonlinear rectification of the Madden–Julian oscillation (Kessler and Kleeman 2000), nonlinearities in the dependence of tropical deep convection on the underlying SST (Hoerling et al. 1997), and the action of phytoplankton as a ''biological thermostat'' (Timmermann and Jin 2002). Yet another possibility is that the positive skewness of SST in the eastern tropical Pacific reflects the positive skewness of the surface zonal wind in the western tropical Pacific (Monahan 2004). The winds in the western tropical Pacific are characterized by westerly bursts, and not easterly ones; the standard stochastic oscillator conception of ENSO (e.g., Penland and Sardeshmukh 1995; Burgers 1999) would then predict stronger El Niños than La Niñas, on average. Of course, all of these mechanisms may play a role in generating the nonlinear structure of ENSO, the understanding of which is an important step in improving our understanding of the ENSO attractor.

Acknowledgments. The authors would like to thank Jonathan Gregory for providing access to the HadCM3 data and Ron Stouffer for the GFDL model data. The HadISST data were provided by the Met Office Hadley Centre. John Fyfe and Bill Merryfield provided helpful comments on an earlier draft of the manuscript. The authors would like to thank two anonymous referees, whose thoughtful comments considerably improved this manuscript. A. Monahan is supported by the Natural Sciences and Engineering Research Council of Canada, by the Canadian Foundation for Climate and Atmospheric Sciences, and by the Canadian Institute for Advanced Research.

REFERENCES

AchutaRao, K., and K. Sperber, 2002: Simulation of the El Niño–Southern Oscillation: Results from the Coupled Model Intercomparison Project. *Climate Dyn.,* **19,** 191–209.

An, S.-I., and F.-F. Jin, 2004: Nonlinearity and asymmetry of ENSO. *J. Climate,* **17,** 2399–2412.

Blackmon, M., and Coauthors, 2001: The Community Climate System Model. *Bull. Amer. Meteor. Soc.,* **82,** 2357–2376.

Burgers, G., 1999: The El Niño stochastic oscillator. *Climate Dyn.,* **15,** 521–531.

——, and D. B. Stephenson, 1999: The ''normality'' of El Niño. *Geophys. Res. Lett.,* **26,** 1027–1030.

Collins, M., S. Tett, and C. Cooper, 2001: The internal climate variability of HadCM3: A version of the Hadley Centre coupled model without flux adjustments. *Climate Dyn.,* **17,** 61–81.

Dai, A., G. Meehl, W. Washington, T. Wigley, and J. Arblaster, 2001: Ensemble simulation of twenty-first-century climate changes: Business as usual versus CO_2 stabilization. *Bull. Amer. Meteor. Soc.,* **82,** 2377–2388.

Davey, M., and Coauthors, 2002: STOIC: A study of coupled model climatology and variability in tropical ocean regions. *Climate Dyn.,* **18,** 403–420.

Delworth, T., R. Stouffer, K. Dixon, M. Spelman, T. Knutson, A. Broccoli, P. Kushner, and R. Wetherald, 2002: Review of simulations of climate variability and change with the GFDL R30 coupled climate model. *Climate Dyn.,* **19,** 555–574.

Ewald, B., C. Penland, and R. Temam, 2004: Accurate integration of stochastic climate models. *Mon. Wea. Rev.,* **132,** 154–164.

Hannachi, A., D. Stephenson, and K. Sperber, 2003: Probability-based methods for quantifying nonlinearity in the ENSO. *Climate Dyn.,* **20,** 241–256.

Hoerling, M. P., A. Kumar, and M. Zhong, 1997: El Niño, La Niña, and the nonlinearity of their teleconnections. *J. Climate,* **10,** 1769–1786.

Hurrell, J. W., and K. E. Trenberth, 1999: Global sea surface temperature analyses: Multiple problems and their implications for climate analysis, modeling, and reanalysis. *Bull. Amer. Meteor. Soc.,* **80,** 2661–2678.

Kalnay, E., and Coauthors, 1996: The NCEP/NCAR 40-Year Reanalysis Project. *Bull. Amer. Meteor. Soc.,* **77,** 437–471.

Kaplan, A., M. Cane, Y. Kushnir, A. Clement, M. Blumenthal, and B. Rajagopalan, 1998: Analyses of global sea surface temperature 1856–1991. *J. Geophys. Res.*, **103,** 18 567–18 589.

Kessler, W. S., and R. Kleeman, 2000: Rectification of the Madden–Julian oscilation into the ENSO cycle. *J. Climate,* **13,** 3560–3575.

Kleeman, R., and A. Moore, 1997: A theory for the limitation of ENSO predictability due to stochastic atmospheric transients. *J. Atmos. Sci.,* **54,** 753–767.

Latif, M., and Coauthors, 2001: ENSIP: The El Niño Simulation Intercomparison Project. *Climate Dyn.,* **18,** 255–276.

Monahan, A. H., 2001: Nonlinear principal component analysis: Tropical Indo-Pacific sea surface temperature and sea level pressure. *J. Climate,* **14,** 219–233.

——, 2004: A simple model for the skewness of global sea surface winds. *J. Atmos. Sci.,* **61,** 2037–2049.

Penland, C., and P. D. Sardeshmukh, 1995: The optimal growth of sea surface temperature anomalies. *J. Climate,* **8,** 1999–2024.

Philander, S. G., 1990: *El Niño, La Niña, and the Southern Oscillation.* Academic Press, 293 pp.

Rayner, N., D. Parker, E. Horton, C. Folland, L. Alexander, D. Rowell, E. Kent, and A. Kaplan, 2003: Global analyses of sea surface temperature, sea ice, and night marine air temperature since the late nineteenth century. *J. Geophys. Res.,* **108,** 4407, doi:10.1029/2002JD002670.

Rodgers, K. B., P. Friederichs, and M. Latif, 2004: Tropical Pacific decadal variability and its relation to decadal modulations of ENSO. *J. Climate,* in press.

Simmons, A., and J. Gibson, 2000: The ERA-40 Project Plan. ERA-40 Project Report Series No. 1, ECMWF, Reading, United Kingdom, 63 pp.

Smith, T. M., and R. W. Reynolds, 2003: Extended reconstruction of global sea surface temperatures based on COADS data (1854–1997). *J. Climate,* **16,** 1495–1510.

——, and ——, 2004: Improved extended reconstruction of SST (1854–1997). *J. Climate,* **17,** 2466–2477.

——, ——, R. E. Livezey, and D. C. Stokes, 1996: Reconstruction of historical sea surface temperatures using empirical orthogonal functions. *J. Climate,* **9,** 1403–1420.

Thompson, C., and D. Battisti, 2000: A linear stochastic dynamical model of ENSO. Part I: Development. *J. Climate,* **13,** 2818–2832.

Timmermann, A., 2003: Decadal ENSO amplitude modulations: A nonlinear paradigm. *Global Planet. Change,* **37,** 135–156.

——, and F.-F. Jin, 2002: Phytoplankton influences on tropical climate. *Geophys. Res. Lett.,* **29,** 2104, doi:10.1029/2002GL015434.

Trenberth, K. E., and D. P. Stepaniak, 2001: Indices of El Niño evolution. *J. Climate,* **14,** 1697–1701.

Washington, W., and Coauthors, 2000: Parallel climate model (PCM) control and transient simulations. *Climate Dyn.,* **16,** 755–774.